Sensors & Actuators: A. Physical 365 (2024) 114889

Contents lists available at ScienceDirect

Sensors and Actuators: A. Physical

journal homepage: www.journals.elsevier.com/sensors-and-actuators-a-physical

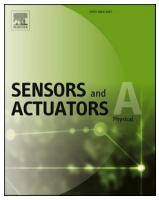

Integrated force and displacement sensing in an untethered dielectric elastomer actuator with a piezoresistive element

Dip Kumar Saha, Hareesh Godaba *

School of Engineering and Informatics, University of Sussex, Falmer, Brighton BN1 9RH, United Kingdom

ARTICLE INFO

Keywords:
Soft robotics
Integrated-sensing
Untethered robots
Piezoresistive sensor
Dielectric elastomer actuators

ABSTRACT

Dielectric elastomer actuators, owing to their fully electrical control and silent operation, are becoming increasingly popular for the development of terrestrial and underwater mobile robots with versatile locomotion capabilities. It is essential to embed the ability to sense their state and external interactions in these robots to facilitate the development of future autonomous capabilities. However, sensorizing dielectric elastomer actuators for untethered robotic applications is challenging due to their use of high voltage and the nonlinear mechanics of the elastomers utilized in them. To address this challenge, we developed a novel technique based on embedded piezoresistive sensing and high voltage feedback to simultaneously estimate the actuator displacement and external force in a fully untethered actuator driven by a miniature low-cost voltage amplifier. A data-driven regression model has been developed to accurately estimate force and displacement from the measured data. Validation tests conducted on three actuators demonstrate promising results. We achieve RMSE values as low as 29.736 mN for force estimation and 0.023 mm for displacement estimation in the zero-voltage condition, where the actuator is subjected to a triangular wave with a mechanical frequency of 0.1 Hz and an amplitude of 3 mm. Additionally, we have realized fully untethered operation by employing a power source, small-size voltage amplifier, microcontroller, and wireless connectivity module embedded in a compact form-factor. This work presents a significant advancement in soft robotics, offering a reliable and cost-effective solution for future autonomous robotic systems based on high-voltage dielectric elastomer actuators.

1. Introduction

Dielectric elastomer actuators (DEAs) have gained significant popularity due to their unique capabilities and potential applications in soft robotics [1]. DEAs exhibit high actuation strain above 100%, allowing large-scale deformations for soft robotic systems [2,3]. They also possess fast response times achieving actuation frequencies in the kilohertz range making them suitable for dynamic applications [4]. The soft and compliant nature of DEAs allows for safe and comfortable physical interactions with humans making them ideal for biomedical devices and prosthetics [5]. Additionally, DEAs are scalable and easily manufacturable through various techniques enabling mass production and customization [6]. Their low power consumption, especially during static actuation enhances energy efficiency in robotics and autonomous systems.

Having these beneficial features, DEAs have emerged as an important contender for the development of soft robots across a wide range of applications. Some of the notable applications based on DEAs are a three fingered gripper made of dielectric elastomer minimum energy structure (DEMES) [7], a six-legged walking robot made of spring-rolled DEAs [8], annelid-inspired earthworm robot [9], a caterpillar-inspired crawling robot [10], a jellyfish-inspired underwater robot [11], a fishlike airship robot [12], a pipeline inspection robot [13], flapping-wing robots [14], soft tuneable lens [15], soft printable hexapod robot [16], etc. These robots need a high voltage (several thousands of volts) power supply, making the system bulky and difficult for untethered operation. Most soft robots using pneumatic or hydraulic power also require a tethered connection to external power supply and control systems, which is a limitation for the robotic systems in rescue operations, underwater deep-sea exploration, and monitoring of environmental conditions [17–19]. To overcome this challenge, onboard electronic control for untethered operation is essential and will open new horizons for soft robotic applications.

Some recent attempts have been made to develop untethered robots [20,21]. Li et al. developed a fast-moving soft electronic fish with a fully integrated power supply and control unit [22]. The untethered

* Corresponding author.
E-mail address: h.godaba@sussex.ac.uk (H. Godaba).

https://doi.org/10.1016/j.sna.2023.114889
Received 1 September 2023; Received in revised form 21 November 2023; Accepted 28 November 2023
Available online 30 November 2023

operation was demonstrated at depths over 3000 m making it possible to explore deep-sea environments for the first time with a soft robot [23]. Cao et al. developed an untethered soft crawling robot, combining DEA and the electrostatic actuation principle [24]. They have used small batteries, portable amplifiers, and wireless communication modules to perform untethered operations. However, none of the untethered robots in literature driven by dielectric elastomer actuators have embedded sensing capability. An integrated sensing technique that does not add significant hardware requirements for instrumentation, is easy to integrate, and compatible with the actuation methods is desirable for the development of future autonomous soft robots driven by dielectric elastomer actuators.

Several self-sensing methods have been proposed in the literature; however, they are unsuitable for untethered operations. A self-sensing DEA based on the capacitance measurement of the DE actuator was an attempt made by Jung et al. in 2008 [25]. Here, two input signals of various frequencies were combined; the high-frequency signal was utilized for sensing and quantifying displacement, while the low-frequency signal was used for actuation. By delivering an arbitrary voltage for a brief length of time, Gisby et al. devised a self-sensing method to measure capacitance [26]. According to the authors, DEA's dynamic behaviour could be examined using the suggested technique. A self-sensing method based on artificial neural networks has been presented in [27], where the actuator displacement was calculated based on the system's change in impedance. Researchers devised an online estimation approach for DE actuator position sensing [28,29]. While many researchers have attempted to devise self-sensing techniques, most of their efforts have been limited to calculating electrical factors like resistance and capacitance to foretell membrane deformation. Zhang et al. developed a novel self-sensing mechanism to detect actuation force in dielectric elastomer actuators [30]. In 2018, Rizzello et al. developed a method to sense force and displacement simultaneously [31]. In this work, the researchers employ the capacitive sensing technique, introducing low-amplitude high-frequency sensing signals into the actuator alongside the input signal. The amplitude of the current at specific frequencies is used to estimate the capacitance and hence the deformation of the actuator. Force estimation is done by the force estimator using voltage and the capacitance measured by a recursive least square (RLS) block. This technique requires a large bandwidth high voltage amplifier to program a precise sensing signal. Such amplifiers are heavy and large making them unsuitable for small-scale or untethered robotic applications.

Several studies also explored the integration of passive sensing elements into dielectric elastomer actuators for the purpose of embedding sensing abilities. O-Brien et al. utilised piezoresistive behaviour of loose-carbon-powder particles to develop a dielectric elastomer actuator with extension sensing and demonstrated qualitative matching with the actual extension [32]. Rosenthal et al. proposed the various sensing modalities available in dielectric elastomer actuators and proposed techniques for measuring electrode resistance and the capacitance of the actuator [33]. More recently, Fasolt et al. studied the effect of screen-printing techniques on the resistance of the electrode and suggested its applicability to sensorizing dielectric elastomer actuators. A study on integrated electroactuators and sensors have shown that passive capacitive sensors used in conjunction with high voltage electroactuators are susceptible to electromagnetic interference and proximity effects, and hence require shielding [34]. Although these studies offer valuable inferences for integrated dielectric elastomer actuator-sensor systems, a compact and fully untethered dielectric elastomer actuator with integrated force and displacement sensing has not been furnished in the literature.

In this work, we have developed a fully untethered soft dielectric elastomer actuator with simultaneous force and displacement measurement capability. We propose an integrated-sensing method that utilises resistance measurements from a piezoresistive sensing track embedded on the elastomer that encodes multi-directional membrane deformation and high voltage feedback to predict the actuator displacement and externally applied force online. Further, we realize fully integrated untethered soft DEA with wireless communication and microcontroller that can input voltage inputs to the actuator and transmit the force and displacement data. This is one of the first approaches for fully untethered integrated-sensing capability in dielectric elastomer actuators which can help pave way for modular dielectric elastomer robots and autonomous operations.

The rest of the paper is organized as follows; Section 2 describes the materials and methods; Section 3 is dedicated to integrated-sensing model development. The experimental results and development of the untethered actuator are discussed in Section 4, and the paper is concluded in Section 5.

2. Materials and methods

2.1. Actuator design

The proposed actuator consists of a pre-stretched elastomer membrane affixed between an inner circular frame and an outer annular frame with a spring lodged between the two to provide an axial preload. An illustration of the developed integrated-sensing actuator with the main components is shown in Fig. 1(A). The outer frame is fabricated by laser cutting an acrylic sheet of 3 mm thickness. The inner diameter of the outer frame is 90 mm. The base, base cover, and inner frames are fabricated by 3D printing using PLA. The outer diameter of the inner frame is 30 mm. The overall size of the proposed actuator including the base cover is 150 mm × 150 mm × 61 mm. Fig. 1(B) shows the exploded view of different layers used for actuator fabrication. Commercially available silicone rubber, Ecoflex™ 00–30, is used as the dielectric elastomer material. Carbon grease 846 from MG chemicals, is used as electrode material for two purposes, actuation electrodes and a resistive sensing track, but with different application methods. Aluminium foil tape is used on top of the inner frame upper, as a connector between two segmented sensor tracks. The detailed fabrication procedure will be discussed later. Fig. 1(C) shows an image of the integrated-sensing actuator prototype along with various terminals for supplying high voltage to the actuator and measuring feedback voltage and resistance from the sensor track. The positive terminal of the high-voltage supply is connected to the bottom layer of the actuator, and the negative terminal is connected to the top layer of the electrode. To make this actuator fully untethered, all the necessary electronic components have been mounted onboard as shown in Fig. 1(D). Arduino Nano has been used as a microcontroller, 9 V Li-ion rechargeable battery is used as power supply, EMCO A60P-5 ultra-miniature DC-High Voltage DC converter with output voltage range 0–6000 V is used for high voltage generation. The high-voltage DC converter used as an amplifier has a maximum output current of 0.16 mA and a low voltage slew rate, limiting its application in high-frequency operations. However, due to its small size, it is well-suited for untethered applications. Finally, an HC-05 Bluetooth module is used for communicating signals between the actuator and remote computer.

2.2. Actuator fabrication

We first fabricate the elastomer membrane that makes up the actuator. Part-A and part-B of Ecoflex™ 00–30 are mixed in equal ratio by weight/volume. For better removal of air bubbles and to reduce the mixture's viscosity, a thinner solution (Smooth-On Silicone Thinner ™) is added, which is 10% of the Part-A and Part-B mixture by weight. The final pre-cure mixture is degassed in a vacuum chamber. The pre-cure mixture is poured into a PVC mould of 100 mm inner diameter and 0.9 mm height and left to cure for four hours at room temperature. For ease of membrane removal from the mould, a thin layer of lubricating oil is sprayed into the mould before pouring the mixture. After curing, the membrane is removed from the mould for further assembly into the

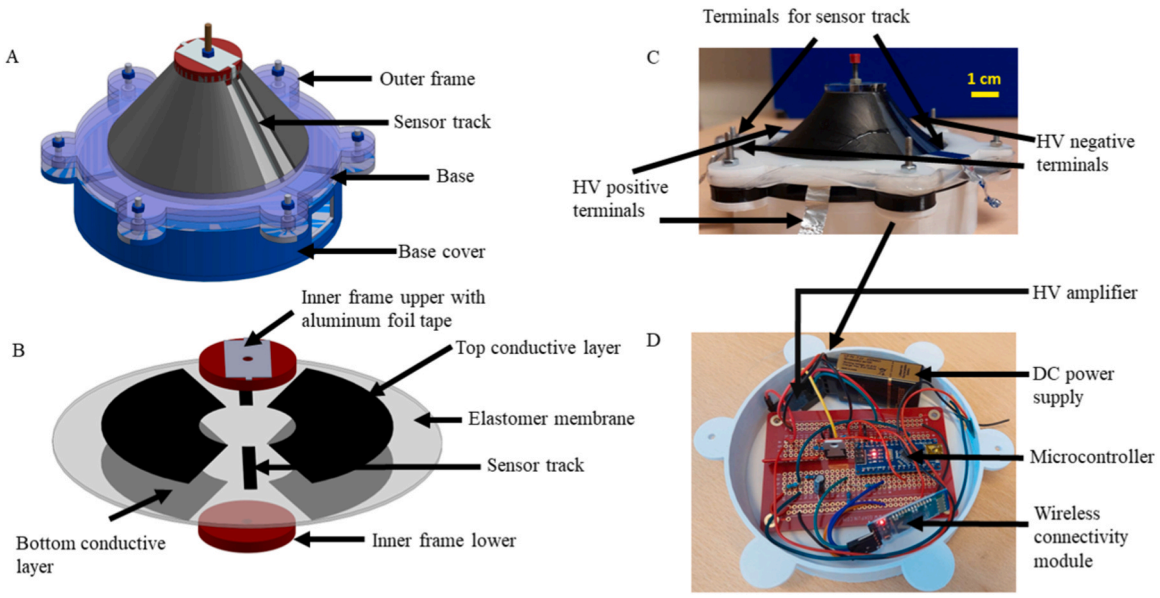

Fig. 1. Integrated-sensing actuator. (A) Complete illustration of proposed integrated-sensing actuator showing all the major components. (B) Exploded view of different layers of actuator construction. (C) Shows the actuator prototype with different terminals used to apply voltage and measure feedback voltage and resistance. (D) Base cover with various electronic components used for untethered operation.

actuator.

The fabricated membrane is equi-biaxially pre-stretched to a prescribed radial pre-stretch and is affixed onto the outer frame as shown in Fig. 2(A). Prestretching improves electromechanical stability and electrical breakdown strength of the membrane. The effect of prestretch on conical actuator design was investigated in [35]. Several pre-stretch ratios have been tested, and finally, a prestretch ratio of 1.5 is fixed for the proposed actuator. This choice was made by the attainment of a linear actuation of 7.28%, a result closely aligned with existing literature [36,37]. The centre of the membrane is marked, and two circular inner frames (inner frame upper and inner frame lower) are firmly attached to the centre of the membrane from the top and bottom using a nuts and bolts as shown in Fig. 2(B). The smearing of the actuation electrodes on both top and bottom layers is shown in Fig. 2(C). In this fabrication step, each electrode is segmented into two equal haves and is painted on both sides of the membrane with the help of a painting brush. An arc of 30 degrees about the centre is left uncoated for coating the sensor track. Carbon grease is used as a compliant electrode material. Carbon grease is a conductive lubricant made of high-purity silicone oil loaded with carbon black particles. In the uncoated region, masking tape is attached to the membrane to produce a track of uniform width of about 4 mm. With the help of a painting brush of a width of 4 mm, a sensor track is smeared using carbon grease. Fig. 2(D) shows the image after coating the senor track. We have used carbon grease as a sensor material due to its advantages over other materials. They are lightweight, stretchable, and easily integrated into various shapes and sizes.

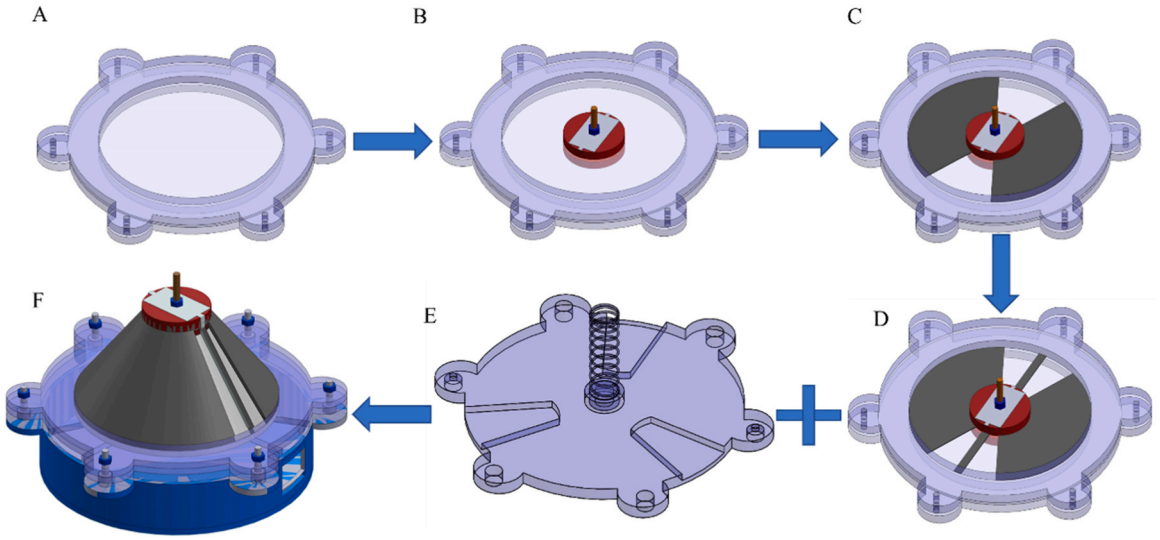

Fig. 2. Actuator fabrication steps from membrane attachment to final assembly. (A) The attachment of pre-stretched elastomer membrane onto the outer frame. (B) Inner frame attachment at the canter of the membrane using hexagon nut (M3) and bolt (M3 *12 mm). Attaching aluminium foil tape on the top of the inner frame upper for connecting two sensor tracks segmented by the inner frame. (C) Coating of top and bottom electrodes with Carbon grease (846–80 G) from MG chemicals keeping about 30 degrees as an uncoated region for coating the sensor track. (D) Coating of sensor track using Carbon grease (846–80 G) from MG chemicals. (E) The attachment of the compression spring as a preloading mechanism to the base of the actuator with hot melt glue. (F) Final assembly of the actuator with base cover including all the electronics components attached onboard using six nuts (M3) and bolts M3 * 12 mm).

When pre-stretched, they are highly sensitive to further changes in membrane strain. Moreover, they are cost-effective and can be applied using simple fabrication techniques. However, one of the main challenges in developing dielectric elastomer carbon grease sensors is the sensor's stability and durability. The carbon grease layer can degrade over time due to environmental factors such as humidity and temperature, which can affect the accuracy and reliability of the sensor. In [38], a thin layer of EcoflexTM 00–30 was coated on top of carbon grease electrodes to prevent deterioration of sensor performance over time. In this work, we employed this technique and coated a thin layer (average thickness of 162 μm) of EcoflexTM 00–30 (mixture of part-A and part-B). This elastomer coating prevents evaporation of the solvent and reduces the mechanical changes in the carbon grease coating thereby improving sensor stability over time. This layer covers only 4.24% area of the membrane's total area and has a negligible effect on overall DE force characteristics. The carbon grease-based sensor also exhibits hysteresis when subjected to cyclic strain. The actuator was subjected to a compressive strain of 3 mm by displacing the actuator tip at the rate of 0.6 mm/s. The hysteresis behaviour of the sensor track is shown in Fig. 3 with the actuator displacement shown on the x-axis and the resistance of the piezoresistive track shown on the y-axis. The maximum hysteresis error in the range of compression is 15.17%. For the actual integrated sensing actuator, this process is conducted after the final assembly as shown in Fig. 2(F). Parallel to the process mentioned in Fig. 2(D), a compression spring with stiffness (0.206 N/mm) is attached to the base of the actuator with the help of hot melt glue as shown in Fig. 2(E). After preloading with the biasing spring, the extra carbon grease deposited on the track was removed with the help of masking tape. While removing extra deposition from the sensor track, a multimeter was connected across the terminals of the sensor track to measure the resistance of the sensor track to maintain the initial resistance in the range of 3–4 MΩ. This range was determined based on trial and error. Experimental trials showed that a lower initial resistance rendered the sensor track less sensitive, while a higher initial resistance made it extremely sensitive and unstable in the higher resistance range. In addition, maintaining a specific initial resistance range allowed us to reuse the same electronic circuitry for readout without having to redesign the electronic circuitry each time a new prototype is fabricated. This is an essential step for obtaining the desired sensitivity of the sensor track. Finally, the assembled actuator is fastened with nuts (M3) and bolts (M3 *12 mm) including all the electronic components mounted to the base cover.

2.3. Sensing mechanism

Simultaneous estimation of both displacement and force involves understanding the deformation characteristics of the sensor track and the corresponding changes in its resistance. However, the deformation characteristics of the sensor track are complex and depend on the applied voltage, the free and blocked condition, displacement range, etc.

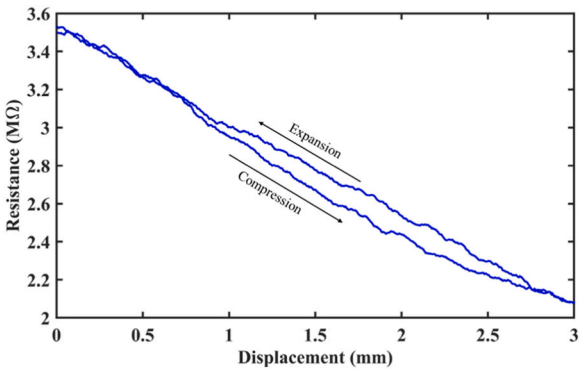

Fig. 3. Hysteresis exhibited by carbon grease sensor during one strain cycle actuated at a 0.1 Hz cyclic frequency.

In this section, we discuss the mechanism of sensing and the various physical scenarios relevant to sensing. In this research, a single piezoresistive track made of carbon grease is embedded in the elastomer membrane to impart sensing ability. When voltage is applied across the actuation electrodes of the actuator, Maxwell stresses are generated in the areal direction. The axial force generated by a biasing mechanism (compression spring) pushes the inner central disc out of the plane and creates a conical shape, resulting in the transformation of the areal expansion of the elastomer to vertical axial expansion.

A key aspect of sensing is to relate the resistance change of the actuator to the actuation strain. However, due to the design of the actuator, the relation between the sensor resistance and the displacement is non-linear and the effect of applied voltage and displacement on the sensor resistance needs to be understood properly. Upon voltage application, different noticeable phenomena are observed during the experiment. The experiments can be categorized into two different cases. One is the free actuation condition when the actuator does not encounter any external force from the environment resisting its extension. The second one is the blocking condition when it is restricted in a specific position and the actuator tip cannot move in the vertical direction.

In the condition of free actuation, the impact of actuation on the resistance of the sensor track is complex due to the interplay between axial and circumferential strains. At low actuation voltage (0–3 kV), the circumferential expansion is dominant over axial expansion; The active region of the actuator expands in the circumferential direction thereby compressing the resistive track circumferentially (in the radial direction). Due to the increase in the areal density of conductive particles, the resistance decreases. That is why a gradual decrease in resistances is observed with an increase in voltage. In the mid-voltage range (3.5–5.5 kV), the axial strain begins to increase counteracting the decrease in resistance due to the circumferential compression of the sensor track. Due to this, although the resistance decreases with increasing voltage, the change is less steep. Above 5.5 kV, with the increase of actuation strain, the axial strain becomes dominant, and an increasing trend in resistances is observed. In the blocking condition, the application of voltages results in a decreasing trend in the sensor's resistance. This is because, in the blocking state, the effect of vertical expansion is absent, as it is fixed at a particular position. Consequently, the active region of the actuator expands in the circumferential direction thereby compressing the resistive track circumferentially (in the radial direction). Due to the increase in the areal density of conductive particles, the resistance decreases. The complete experimental characterization for both free actuation and isometric force conditions are shown in Fig. 6 and Fig. 7. The angle of the uncoated region has a significant impact on the physical phenomenon mentioned above. Too high an angle of the uncoated region is unsuitable for actuation performance as it reduces the effective active zone of the actuator. Too low an angle makes the circumferential expansion on the track dominant making it less sensitive to the axial expansion. An optimum angle (30 degrees in this proposed design) of the uncoated region is conducive for the development of a clear pattern in resistance change upon voltage application.

The selection of appropriate material for the sensor track is important as the material simultaneously needs to be sensitive and compliant with the elastomer material as well as be robust for a large number of actuation cycles. We also tested a commercial conductive fluoroelastomer, Electrodag® 502, as the sensor material. It has good sensitivity with a wide range of resistance change due to strain which is useful for sensing. However, the stretchability of cured Electrodag® 502 is limited and the sensor track develops cracks upon repeated expansion. The sensitivity continues to increase, making this material unreliable for the resistive track. Coating a layer of Ecoflex™ 00–30 as a protective layer on top of the Electrodag® 502 causes the resistive track loses its conductivity entirely because the Ecoflex layers trapped inside the cracks act as an insulating medium. This indicates that the choice of stretchable

conductor for the development of the embedded sensing capability is important for performance and reliability.

3. Data-driven integrated-sensing model

We adopt a data-driven approach to develop an integrated-sensing model to simultaneously estimate force and displacement from the voltage and resistance data. A data-driven regression model is a statistical method that utilizes past observations or experiments to establish relationships between input variables or factors and predict numerical values based on them. The concept is initialized because the displacement and force generated by a dielectric elastomer actuator are related to the applied voltage. In Fig. 4, the block diagram represents the general architecture of the simultaneous integrated-sensing algorithm. When voltage is applied to the actuator, it actuates and a corresponding change in resistance in the embedded sensor is observed. Measuring these resistance changes along with the feedback voltages, data-driven force and displacement prediction models are developed. We represent the predicted force $F_{predicted}$ and predicted displacement $d_{predicted}$, by the following equations:

$$F_{predicted} = f\left(R, V_{fb}\right) \tag{1}$$

$$d_{predicted} = f\left(F_{predicted}, R, V_{fb}\right) \tag{2}$$

where, R is resistance and V_{fb} is feedback voltage. Feedback voltage is the voltage across the two electrodes of the actuator measured utilizing a voltage-divider circuit.

3.1. Gaussian process regression (GPR)

Gaussian process regression is a non-parametric Bayesian approach to regression analysis that uses a Gaussian process to model the relationship between input variables and output variables. The model assumes that the output variable is a function of the input variable with some random noise. This function is modelled as a distribution over functions, where its mean and covariance functions specify each function [39], [40]. Mathematically, the Gaussian process regression model can be written as follows:

$$f(x) = Gp(m(x), k(x, x^{'}))) \tag{3}$$

where, $f(x)$ is the predicted value of the dependent variable, $m(x)$ is the mean function, and $k(x, x^{'})$ is the covariance function or kernel. The kernel specifies the covariance between any two points in the input space.

For our specific problem, we model F as a function of R and V using GPR:

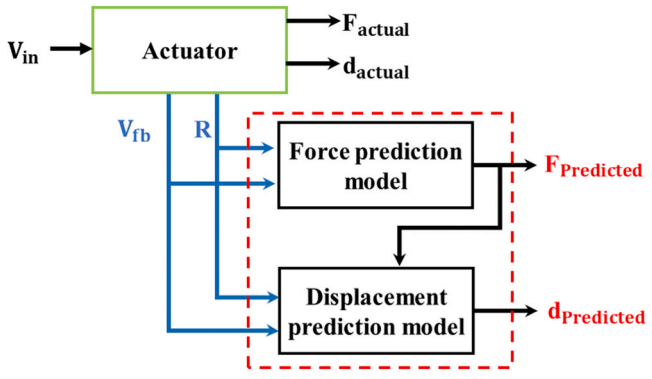

Fig. 4. Block diagram of the model for simultaneous sensing of force and displacement taking resistance and feedback voltage as independent variables.

$$F(R, V) = Gp(m(R, V), k((R, V), (R^{'}, V^{'}))) \tag{4}$$

Once we have predicted F using GPR, we use it as an additional input to model d as a function of R, V, and F:

$$d(R, V, F) = Gp(m(R, V, F), k((R, V, F), (R^{'}, V^{'}, F^{'}))) \tag{5}$$

3.2. Model performance evaluation metrics [41]

3.2.1. Root mean squared error (RMSE)

The RMSE is a measure of the average deviation of the predicted values from the actual values. It is defined as the square root of the average of the squared differences between the predicted values and the actual values.

$$RMSE = \sqrt{\frac{1}{n}\sum_{i=1}^{n}(y_i - \widehat{y_i})^2} \tag{6}$$

where n is the number of observations, y_i is the actual value for the i^{th} observation, and $\widehat{y_i}$ is the predicted value for the i^{th}observation.

3.2.2. Coefficient of determination (r^2)

The r^2 value is a measure of how well the regression model fits the data. It represents the proportion of the variance in the dependent variable that is explained by the independent variables. It is defined as:

$$r^2 = 1 - \frac{\sum_{i=1}^{n}(y_i - \widehat{y_i})^2}{\sum_{i=1}^{n}(y_i - \bar{y})^2} \tag{7}$$

where n is the number of observations, y_i is the actual value for the i^{th} observation, and $\widehat{y_i}$ is the predicted value for the i^{th} observation, and $\bar{y}$ is the mean of the actual values. The r^2 value ranges from 0 to 1, with higher values indicating a better fit of the model to the data.

3.3. Experimental setup and data collection

An experimental setup has been designed to conduct comprehensive characterization and validation tests. For the characterization tests, a Heinzinger LNC 10000–5 high-voltage DC power supply is utilized. This amplifier is capable of providing precise voltages up to 10 kV and has efficient discharge capabilities. It is operated in internal mode using a manual knob for ease of control. The experimental platform, as shown in

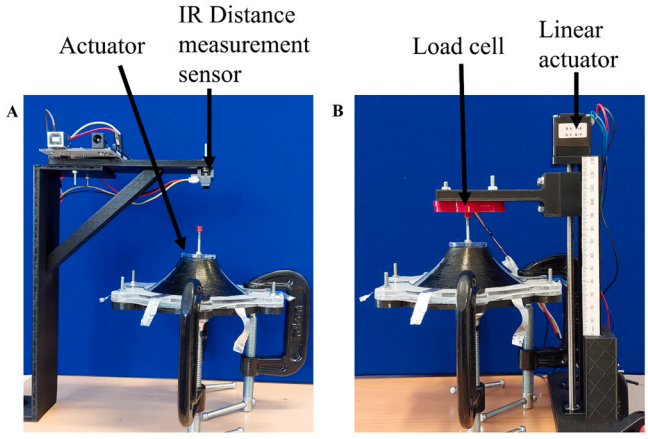

Fig. 5. Experimental setup. (A) Illustrates the configuration for displacement measurement using an IR displacement measurement sensor. (B) Depicts the experimental setup designed for force characterization tests. It includes a load cell and a linear actuator utilized for conducting validation tests at varying mechanical frequencies and displacement amplitudes.

Fig. 5, is designed to investigate the isometric force characteristics when voltage is applied. A linear actuator (NEMA11 Stepper Motor) with an effective length of 150 mm is employed for this purpose. The actuator is driven by a TB6600 stepper motor driver, programmed through an Arduino microcontroller to apply specific displacements to the actuator's tip. To measure the force generated by the actuator upon voltage application, an FX29 compact compression load cell is integrated with the linear actuator using a 3D-printed I-beam as shown in Fig. 5(B). For monitoring vertical displacement during free actuation conditions, a Sharp IR distance measurement sensor GP2Y0A41SK0F is employed shown in Fig. 5(A). Additionally, to measure the resistance and feedback voltage, a customized circuit is constructed using a microcontroller. To measure the resistance of the sensor track, a voltage-divider circuit is constructed. The sensor track is connected in series with a 10 MΩ resistor, and the free end of the 10 MΩ resistor is connected to the 5 V pin of the Arduino and the voltage at the junction between the sensor track and the large resistor is measured. To reduce noise in the resistance measurements, a low-pass filter consisting of a 100 kΩ resistor and a 0.1 μF capacitor was incorporated in parallel to the sensor track. As the DC-High Voltage DC converter for untethered operation has an amplification gain that changes with the load, we also assemble a voltage feedback circuit to measure the actual output voltage across the electrodes rather than relying on the input voltage from the microcontroller. To measure the feedback voltage across the actuator electrodes, another voltage divider circuit comprising a 200 MΩ resistor and a 100 kΩ resistor in parallel to the actuator electrodes was utilized. The feedback voltage was then measured across the 100 kΩ resistor. This experimental setup allows for a comprehensive characterization of the actuator's behaviour under different conditions.

We experimentally record the data for force, actuator displacement, sensor resistance, and feedback voltage for different applied voltages in three different experimental cases. The first is the free actuation condition, in which the top end of the actuator is unobstructed and free to move. In this case, the force is considered to be zero, and the actuator displacement is measured using the IR displacement measurement sensor. In the second case, we measure isometric forces applied by the actuator at different actuator displacements. A force sensor is fixed at a specific distance from the actuator tip (1 mm and 2 mm). When the voltage applied to the actuator is increased, the actuator actuates freely until it is obstructed by the force sensor, after which the actuator displacement is fixed, and the force begins to increase. Lastly, in the third case, we compress the actuator at different positions, ranging from 0 mm to 4 mm in 1 mm steps. We measure the actuator blocking forces and corresponding resistances under these compression conditions. Data is collected for a voltage range of (0–7.5 kV) for all the cases.

The experimental data for force plotted against voltage and resistance is depicted in Fig. 6. The application of voltages ranging from 0 kV to 7.5 kV results in a resistance changes between 2 and 4.3 MΩ. This voltage range corresponds to a maximum blocking force of approximately 1550 mN. The graph exhibits a horizontal zero-force line, which corresponds to movement of the actuator in the free actuation condition. In the blocking condition, where the actuator is compressed at various positions, the force shows an increasing trend as the dielectric elastomer releases tension upon voltage application. Simultaneously, a decreasing trend in resistance is observed for a specific compressed position due to the influence of circumferential expansion on the sensor track. Fig. 7 shows the experimental data for displacement plotted against voltage and resistance. It clearly shows an increasing trend in displacement with increasing voltage, reaching a maximum displacement of 2.91 mm at 7.5 kV. During the compression of the actuator from the 2 mm to 3 mm position, a change in resistance is observed, ranging from 2.75 MΩ to approximately 2.20 MΩ. This change in resistance is attributed to the decrease in inter-particle distance between the carbon grease particles dispersed within the sensor track. This experimental data is later used for fitting the data-driven model to predict displacement and force based on voltage and resistance data measured simultaneously from the actuator prototype.

3.4. Fitting of regression model

The experimental data collected is utilized to train the Gaussian process regression model using MATLAB's Machine Learning and Deep Learning toolbox. To ensure the model's generalization and avoid overfitting, a 5-fold cross-validation strategy is implemented for both force and displacement prediction models. The Gaussian process regression model utilized a single exponential kernel. The selected configuration involved an isotropic kernel with an automatic kernel scale and sigma setting. For the force prediction model, we consider voltage and resistance data as inputs for model fitting, while the output force data from the force prediction model along with the voltage and resistance data is used as input to develop the displacement prediction model. Fig. 8 and Fig. 9 depict the model performance plots for force and displacement prediction, respectively, illustrating reasonable fitting performance. Table 1 summarizes the model performance results. In the force prediction model, Actuator-2 exhibits the best Root Mean Squared Error (RMSE) of 15.398 mN, while Actuator-1 shows the maximum RMSE of 65.453 mN. It is worth noting that the force measuring range spans from 0 to 1620 mN. In the displacement prediction model, Actuator-1 demonstrates the minimum RMSE value of 0.0167 mm, and Actuator-2 exhibits the maximum RMSE of 0.0398 mm. The displacement measuring range extends from −4 mm to 2 mm. The R-squared values are predominantly close to 1 across the models, indicating a high level of accuracy in fitting the model data to the experimental data. The inclusion of force data as an input parameter for displacement prediction performed better in comparison to the model considering only resistance

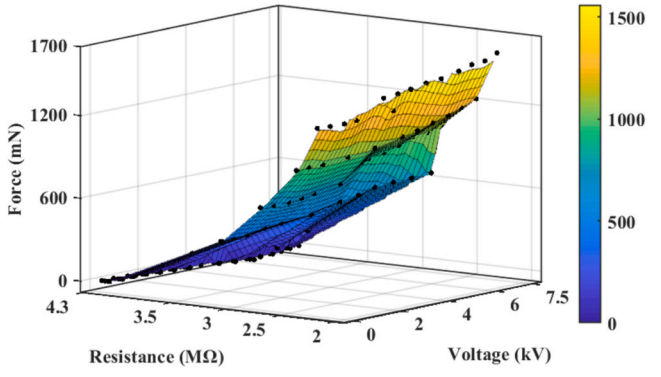

Fig. 6. The 3D surface plot showcases the relation between force (Z-axis), resistance (X-axis), and voltage (Y-axis) in the experimental characterization of the actuator in three different cases.

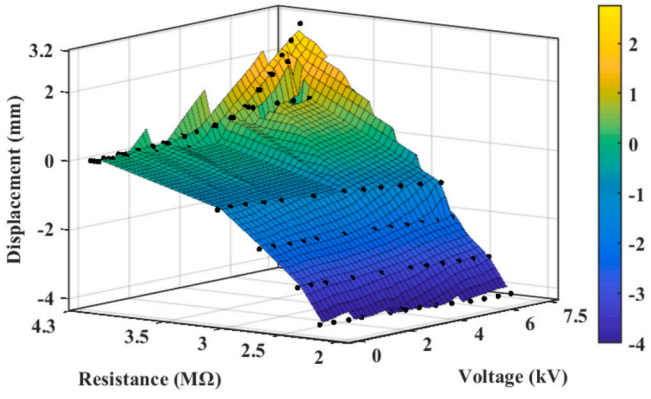

Fig. 7. The 3D surface plot shows the relation between displacement (Z-axis), resistance (X-axis), and voltage (Y-axis) in the experimental characterization of the actuator in three different cases.

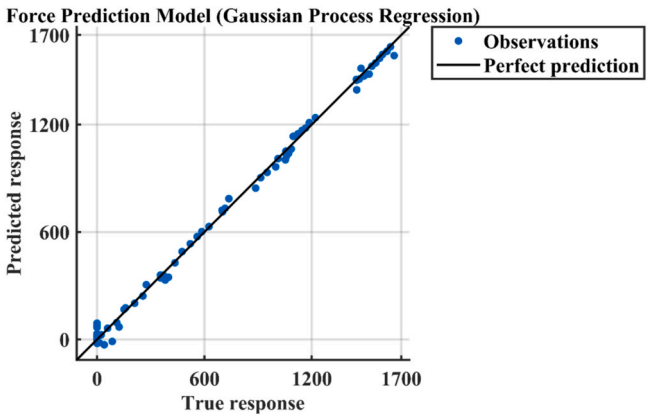

Fig. 8. The plot showcases the model's precise estimation of forces, with the x-axis representing the true response and the y-axis representing the predicted response. The solid black line denotes the model's mean prediction, while the blue dots illustrate the observations.

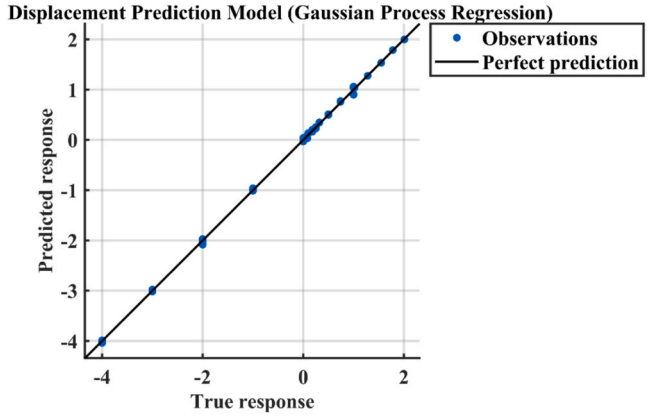

Fig. 9. The plot showcases the model's precise estimation of displacements, with the x-axis representing the true response and the y-axis representing the predicted response. The solid black line denotes the model's mean prediction, while the blue dots illustrate the observations.

Table 1
Model performance results of each individual actuator.

Name of actuator	Test conditions	RMSE	r-squared
Actuator-01	Force prediction (0 to −3 mm) Force prediction (1 to −1.5 mm)	29.736 mN	1.00
	Displacement prediction (0 to −3 mm) Displacement prediction (1 to −1.5 mm)	0.023 mm	1.00
Actuator-02	Force prediction (0 to −3 mm) Force prediction (1.5 to −1.5 mm)	65.453 mN	0.99
	Displacement prediction (0 to −3 mm) Displacement prediction (1.5 to −1.5 mm)	0.0661 mm	1.00
Actuator-03	Force prediction (0 to −3 mm) Force prediction (1 to −1.5 mm)	15.398 mN	1.00
	Displacement prediction (0 to −3 mm) Displacement prediction (1 to −1.5 mm)	0.041 mm	1.00

and feedback voltage as the model inputs. We attribute this to the large influence of the axial versus circumferential expansion of the membrane on sensor resistance which is directly linked to whether the actuator is in the free or blocked condition.

4. Results and discussions

4.1. Model validation

The validation tests have been performed under various operating conditions, including scenarios with or without voltage, different frequencies, and different mechanical displacements. In the zero-voltage condition, the actuator is subjected to a triangular wave with a mechanical frequency of 0.1 Hz and an amplitude of 3 mm (ranging from 0 to −3 mm). For this experiment, a load cell is connected to measure the force, while displacement data are collected from the linear actuator by counting the micro-stepping of the stepper motor. Data collection is performed for three complete operating cycles. Subsequently, a simple moving average filter is employed to preprocess the resistance data and remove random noise from the signal. The pre-processed dataset is then fed into the trained Gaussian Process Regression (GPR) model for force and displacement prediction purposes. Fig. 10 and Fig. 11 depict the force and displacement predictions, respectively, for the no-voltage condition. In the second case, a constant 6 kV voltage is applied to the actuator. Subsequently, the actuator is subjected to a triangular wave with a mechanical frequency of 0.1 Hz and a mechanical displacement of 2.5 mm (ranging from 1 to −1.5 mm). Fig. 12 and Fig. 13 illustrate the force and displacement predictions for the condition with voltage. To verify the repeatability and effectiveness of the methodology for force and displacement sensing, validation tests are conducted on two additional actuators. Actuator-2 is tested with a mechanical frequency of 0.02 Hz, while Actuator-3 is tested with a mechanical frequency of 0.1 Hz. Table 2 provides a comprehensive summary of the validation results for all three actuators. The evaluation metrics used for model validation are explained in Section 3.2 of the paper. The force prediction model attained a lowest RMSE of 42.54 mN. Regarding displacement prediction, the lowest RMSE achieved was 0.1180 mm. Table 3 summarizes the results for 0.2 Hz frequency. At this frequency, RMSE obtained for force estimation is 130.65 mN and 0.31 mm for displacement estimation. At higher frequencies, the estimation accuracy starts to decrease significantly.

Validation test is also conducted to predict the force during the actuator's interaction with external environment. In this experiment, the actuator is initially compressed by 2 mm from the actuator tip using the linear actuator and maintained in that position throughout the test. A high bandwidth high voltage amplifier, Ultravolt HVA-10, is used to generate time-varying voltage signals. Specifically, square wave signals with amplitudes of 3 kV, 4 kV, and 5 kV are applied, as depicted in the top plot of Fig. 14. During this experiment, resistance and feedback

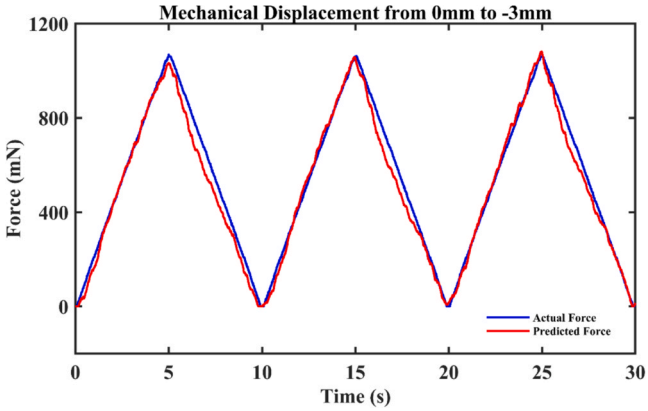

Fig. 10. Force prediction resulting from the application of a unipolar triangular input displacement of 3 mm with a frequency of 0.1 Hz, while applying zero voltage to the proposed integrated-sensing actuator.

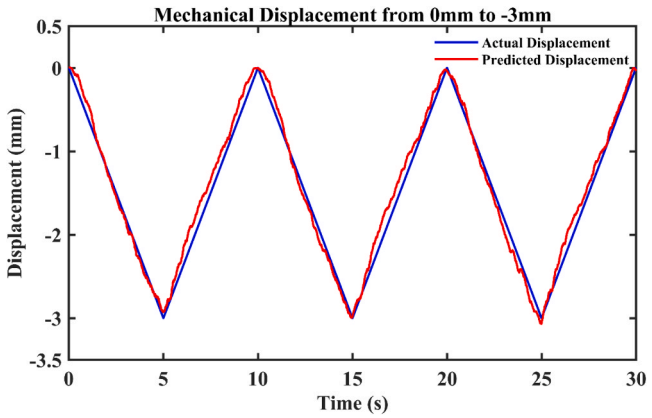

Fig. 11. Displacement prediction resulting from the application of a unipolar triangular input displacement of 3 mm with a frequency of 0.1 Hz, while applying zero voltage to the proposed integrated-sensing actuator.

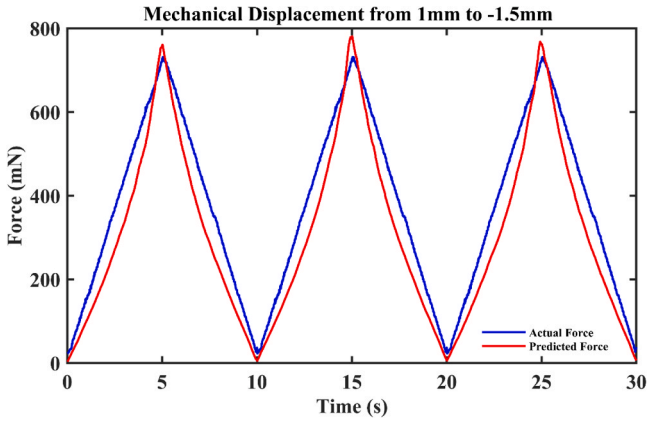

Fig. 12. Force prediction resulting from the application of a unipolar triangular input displacement of 2.5 mm with a frequency of 0.1 Hz, while applying a voltage of 6000 V to the proposed integrated-sensing actuator.

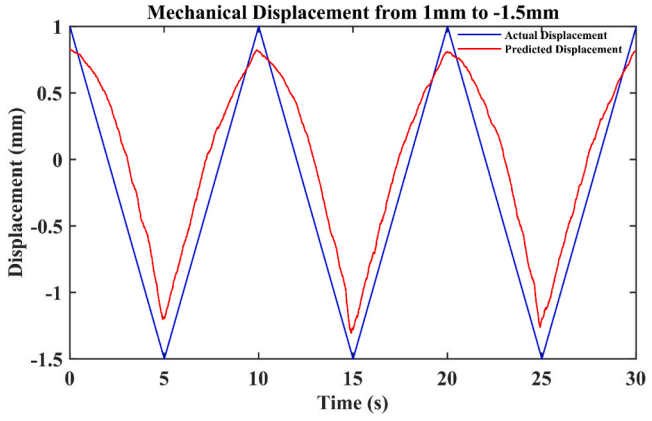

Fig. 13. Displacement prediction resulting from the application of a unipolar triangular input displacement of 2.5 mm with a frequency of 0.1 Hz, while applying a voltage of 6000 V to the proposed integrated-sensing actuator.

voltage data are collected, and force is estimated using the trained model. The bottom plot of Fig. 14 displays the prediction results along with the measured values obtained from the load cell. The estimation results show an RMSE of 48.2957 mN. Notably, the prediction curve closely aligns with the actual force curve in the steady state. However, the transient response indicates that the estimation takes 1–2 s to settle

Table 2
Model validation results of each individual actuator 0.1 Hz.

Name of actuator	Test condition	RMSE
Actuator-01	Force prediction (0 to −3 mm)	42.54 mN
	Force prediction (1.5 to −1.5 mm)	73.91 mN
	Displacement prediction (0 to −3 mm)	0.1180 mm
	Displacement prediction (1.5 to −1.5 mm)	0.3112 mm
Actuator-02	Force prediction (0 to −3 mm)	72.99 mN
	Force prediction (1.5 to −1.5 mm)	96.57 mN
	Displacement prediction (0 to −3 mm)	0.2364 mm
	Displacement prediction (1.5 to −1.5 mm)	0.3281 mm
Actuator-03	Force prediction (0 to −3 mm)	77.43 mN
	Force prediction (1.5 to −1.5 mm)	53.117 mN
	Displacement prediction (0 to −3 mm)	0.2392 mm
	Displacement prediction (1.5 to −1.5 mm)	0.2392 mm

Table 3
Model validation results of the actuator at 0.2 Hz with no voltage condition.

Test condition	RMSE
Force prediction (0 to −3 mm)	130.65 mN
Displacement prediction (0 to −3 mm)	0.31 mm

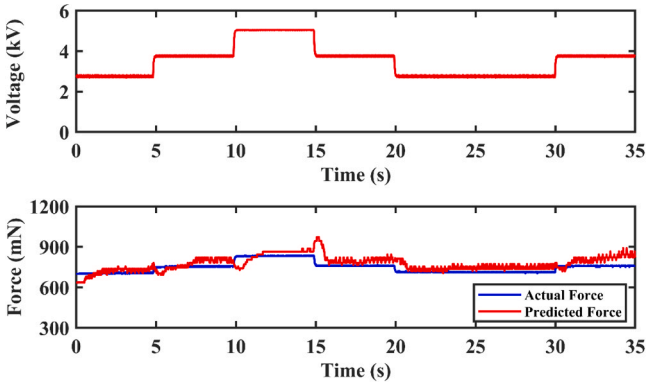

Fig. 14. Force prediction at a deformed condition where actuator is compressed 2 mm from the actuator tip and a square wave of variable voltages (3000 V. 4000 V, and 5000 V) are applied to the actuator with a frequency of 0.2 Hz.

to the steady state estimated value. In some cases, such as during the sudden change in voltage from 5 kV to 4 kV, there is an abrupt rise in the predicted force. There is scope for further investigation of the sensing circuitry to improve the estimation of force in dynamic conditions. The results explained above indicate the model's reliability and suitability for predicting force and displacement under varying voltage conditions.

4.2. Repeatability tests

The repeatability test has been performed in two cases which are explained below:

4.2.1. Free actuation

This experiment aims to verify the consistency of the sensor track of proposed integrated-sensing actuator during continuous cyclic operation in free actuation conditions. In this experiment, the actuator is subjected to cyclic actuation by applying a 6 kV voltage on-off input for 800 times (5 s on and 5 s off). The behaviour of the resistive sensor track is carefully observed throughout the experiment. The top plot of Fig. 15 shows the feedback voltage and the bottom plots show the resistance data for the three sets of ten cycles. The blue curve shows the resistance data over the first 10 cycles, the black curve for 401–410 cycles, and the green curve for 791–800 cycles. During the initial ten cycles, the mean

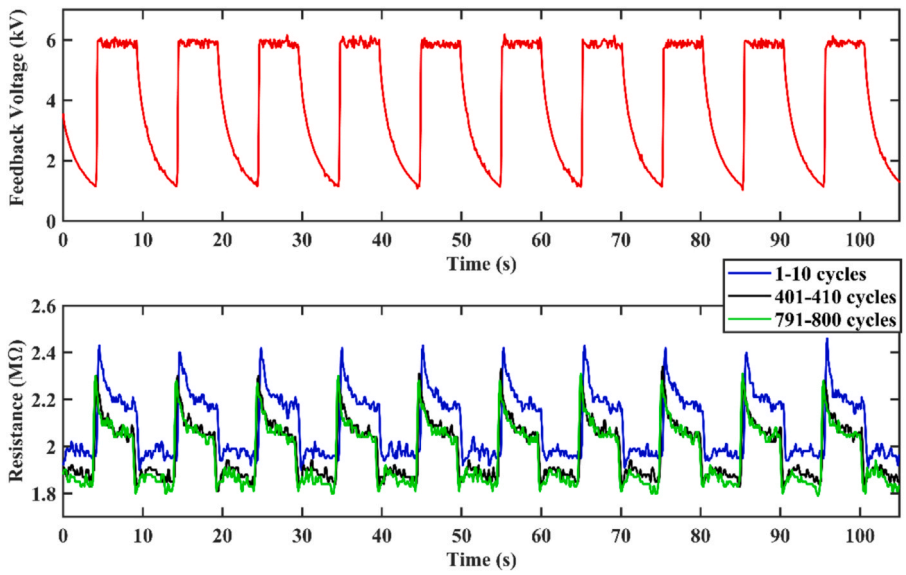

Fig. 15. Repeatability test for free actuation condition where a cyclic voltage was applied to the actuator 800 times. Upper plot shows the feedback voltage, while lower plots show the measured resistance from three different regions.

peak resistance of the sensor track was recorded as 2.421 MΩ (blue curve). In 800 cycles, only a slight drift is observed, where the mean peak resistance value reduces to 2.288 MΩ (green curve) for the last ten cycles. The overall deviation for mean peak resistance was 5.49%. The deviations for voltage ON state and voltage OFF state are 5.94% and 5.48% respectively. The drift in resistance value decreases with time with the difference between the resistance around in the middle and last cycles being very negligible. This change of resistance over time in free actuation condition is similar to the mechanical creep typically observed in viscoelastic materials. Addressing this drift through history dependent models is an interesting area for further investigation. The actuator operates smoothly without any noticeable discontinuities, as evident from both figures. A small portable amplifier was employed to ensure the actuator's programmable operation during the experiment. However, this portable amplifier doesn't have any inbuilt internal discharging circuit. Consequently, an auxiliary resistor of 1000 MΩ is incorporated parallelly to facilitate discharging, resulting in an increased RC time constant. It should be noted that the voltage curve in both figures indicates the actuator starts again before reaching zero, as the discharging cycle was not yet finished. This experiment successfully demonstrates the reliable performance of the integrated-sensing actuator and the consistent behaviour of the resistive sensor track, even during prolonged and continuous actuation cycles.

4.2.2. *Mechanical deformation by linear actuator*

In this experiment, the actuator undergoes continuous mechanical deformation using linear actuator without the application of voltage. The actuation was conducted at a frequency of 0.4 Hz with a displacement amplitude of 3 mm for a duration of 2500 s, comprising about 1000 cycles. Fig. 16 presents the data obtained from the first and last ten cycles. From Fig. 16(A), it is evident that the peak resistance occurs at approximately 2.5 MΩ. However, after subjecting the actuator to 990 cycles of continuous mechanical deformation, the peak resistance value has shifted to around 2.35 MΩ, representing a deviation of approximately 6% shown in Fig. 16(B). Due to electromagnetic interference (jittering effect) of the linear stepper actuator some noise is observed in the sensor data that is evident in both the curves. The results indicate that continuous mechanical deformation without voltage application has limited effect on the resistive properties of the actuator. The observed resistance drift demonstrates the need for careful consideration when employing the actuator under mechanical deformation for long time operation.

4.3. *Demonstration of untethered operation*

From the validation results, it is evident that the data-driven model developed in this study can accurately estimate the force and displacement for the proposed integrated-sensing actuator. With these promising outcomes, we demonstrate its real-time application, particularly for

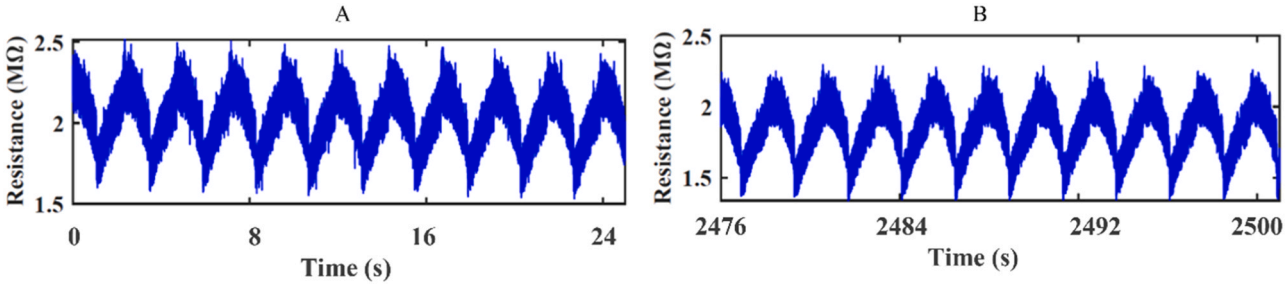

Fig. 16. Repeatability test for actuation at a blocked condition where the actuator is deformed mechanically to a fixed displacement of 3 mm. (A) First Ten Cycles of Actuation: This section displays the data from the initial ten cycles of actuation, showcasing the actuator's response and sensor behaviour during the early stages of the repeatability test. (B) Last Ten Cycles of Actuation Data: This portion presents the data obtained from the final ten actuation cycles, providing insights into the actuator's response and sensor behaviour towards the end of the repeatability test.

untethered operation. To demonstrate this, we have developed a fully untethered actuator equipped with an onboard power source, high-voltage amplifier, microcontroller, and a wireless communication module. This configuration allows us to program the input voltage and obtain the force and displacement feedback to a computer wirelessly. The untethered operation is enabled by including an HC-05 Bluetooth module, which pairs with a laptop with built-in Bluetooth capabilities. We use a 9 V Lithium-ion battery to power the Arduino Nano microcontroller and the miniature high-voltage amplifier (EMCO A60P-5). A program is created using Arduino IDE to program input actuation signals, conduct sensor data reading and Bluetooth communication. Force and displacement estimation and data visualization are performed in MATLAB on the remote computer using the trained model developed previously. Fig. 17 shows image sequences from the real-time demonstration of the untethered operation of the integrated-sensing actuator. Here, the actuator is operated remotely without any wired connection. Fig. 17(A) depicts the actuator before any external force is applied, showing a gap between the actuator tip and the finger. The signal line for both the estimated force and displacement are flat, indicating that no external force is applied to the actuator. When the finger is pressed against the actuator tip (denoted by a shaded region in the graphs), deformation occurs resulting in gradual changes in displacement and a

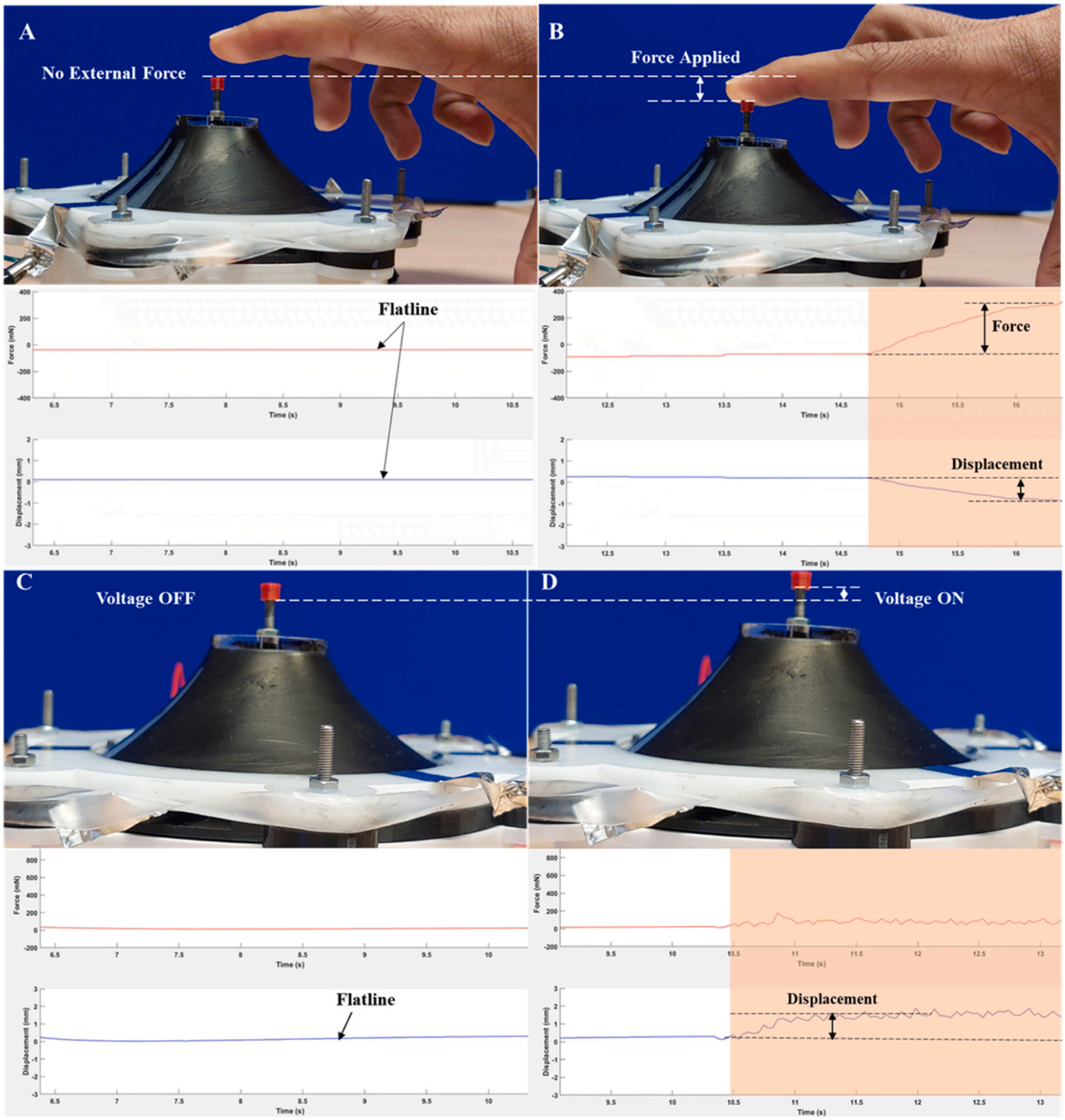

Fig. 17. Real-time demonstration of the untethered operation of the proposed integrated-sensing actuator. (A) Initial Configuration: A distinct gap between the finger and actuator tip is visible, and the signal line remains flat, indicating no external force is applied. (B) External Interaction: Upon pressing the finger against the actuator, a gradual increase in force is observed, leading to a corresponding decrease in displacement. (C) Voltage OFF State: With the voltage turned off, the signal lines remain flat, illustrating that the actuator is not actively engaged. (D) Voltage ON State: As soon as voltage is applied to the actuator, a change in displacement signal is observed while the force signal remains flat indicating no external force is applied.

corresponding increase in force, as depicted in Fig. 17(B). This figure shows a negative sign on the vertical axes representing actuator compression. Fig. 17(C) shows the actuator without any external contact and no voltage applied to it. The estimated force and displacement curves remain flat as the actuator is not yet actuated. Fig. 17(D) depicts the voltage ON state. As soon as voltage is applied to the actuator (depicted by shaded region in the graph), a corresponding change in displacement (indicated by the two black dotted lines) is observed while the force signal remains close to zero indicating no external force is applied. The comprehensive set of results in Fig. 16 elucidate how the proposed integrated-sensing actuator senses displacement and force under both mechanical and electrical stimuli.

5. Conclusion

This paper presents a novel methodology for integrating sensing capabilities into untethered dielectric elastomer actuators through embedding a piezoresistive sensing track and measuring high voltage feedback. Through the development of a data-driven model, we demonstrated good accuracy in estimating both force and actuator displacement under various operating conditions. By addressing the challenges associated with nonlinear behaviour of dielectric elastomer materials, this research contributes to advancing sensorless control in soft robotics. The utilization of a small-size amplifier, battery, and wireless module has enabled the development of a completely untethered soft actuator that can receive input signals and communicate its state and external physical interactions wirelessly. This study serves as the initial proof-of-concept for embedding sensing capability in soft actuator and further investigations are necessary to explore its practical implications in real robotic systems.

The DC - high voltage DC converter used in this study exhibits low voltage slew-rate limiting the application of this actuator to low frequency actuation. In addition, the actuator characterization data for training the model as well as the force and displacement estimation models consider steady state conditions. However, viscoelasticity of the elastomer membrane is expected to influence the force estimation in dynamic conditions. While, the proposed integrated sensing method has shown effective functionality in the sub-Hz frequency, there remains room for improvement in high voltage generation, electronic circuitry with larger bandwidth, as well as the models for force and displacement estimation for higher frequency applications. Future work considering dynamic conditions for obtaining training data and time-dependent models to capture dynamic behaviour would be of significant interest. Furthermore, we will work towards optimizing and combining multiple modules of these untethered actuators to develop functional soft robots that capable of feedback control and semi-autonomous operations.

CRediT authorship contribution statement

Godaba Hareesh: Conceptualization, Methodology, Project administration, Resources, Supervision, Writing – original draft, Writing – review & editing. **Saha Dip Kumar:** Investigation, Methodology, Validation, Visualization, Writing – original draft, Writing – review & editing.

Declaration of Competing Interest

The authors declare that they have no known competing financial interests or personal relationships that could have appeared to influence the work reported in this paper.

Data Availability

No data was used for the research described in the article.

References

[1] M. Franke, A. Ehrenhofer, S. Lahiri, E.F.M. Henke, T. Wallmersperger, A. Richter, Dielectric elastomer actuator driven soft robotic structures with bioinspired skeletal and muscular reinforcement, Front Robot AI 7 (2020), https://doi.org/10.3389/frobt.2020.510757.
[2] M. Kollosche, J. Zhu, Z. Suo, G. Kofod, Complex interplay of nonlinear processes in dielectric elastomers, Phys. Rev. E Stat. Nonlin Soft Matter Phys. 85 (2012), https://doi.org/10.1103/PhysRevE.85.051801.
[3] Y.F. Goh, S. Akbari, T.V. Khanh Vo, S.J.A. Koh, Electrically-induced actuation of acrylic-based dielectric elastomers in excess of 500% strain, Soft Robot 5 (2018) 675–684, https://doi.org/10.1089/soro.2017.0078.
[4] E. Hajiesmaili, D.R. Clarke, Dielectric elastomer actuators, J. Appl. Phys. 129 (2021), https://doi.org/10.1063/5.0043959.
[5] M. Li, A. Pal, A. Aghakhani, A. Pena-Francesch, M. Sitti, Soft actuators for real-world applications, Nat. Rev. Mater. 7 (2022) 235–249, https://doi.org/10.1038/s41578-021-00389-7.
[6] S. Rosset, H.R. Shea, Towards fast, reliable, and manufacturable DEAs: miniaturized motor and Rupert the rolling robot, in: Electroactive Polymer Actuators and Devices (EAPAD) 2015, SPIE, 2015: p. 943009. https://doi.org/10.1117/12.2085279.
[7] G. Kofod, W. Wirges, M. Paajanen, S. Bauer, Energy minimization for self-organized structure formation and actuation, Appl. Phys. Lett. 90 (2007) 1–4, https://doi.org/10.1063/1.2695785.
[8] Q. Pei, M. Rosenthal, S. Stanford, H. Prahlad, R. Pelrine, Multiple-degrees-of-freedom electroelastomer roll actuators, Smart Mater. Struct. 13 (2004), https://doi.org/10.1088/0964-1726/13/5/N03.
[9] K. Jung, J.C. Koo, J. Do Nam, Y.K. Lee, H.R. Choi, Artificial annelid robot driven by soft actuators, Bioinspir Biomim. 2 (2007), https://doi.org/10.1088/1748-3182/2/2/S05.
[10] E.F.M. Henke, S. Schlatter, I.A. Anderson, Soft dielectric elastomer oscillators driving bioinspired robots, Soft Robot 4 (2017) 353–366, https://doi.org/10.1089/soro.2017.0022.
[11] H. Godaba, J. Li, Y. Wang, J. Zhu, A soft jellyfish robot driven by a dielectric elastomer actuator, IEEE Robot Autom. Lett. 1 (2016) 624–631, https://doi.org/10.1109/LRA.2016.2522498.
[12] C. Jordi, S. Michel, E. Fink, Fish-like propulsion of an airship with planar membrane dielectric elastomer actuators, Bioinspir Biomim. 5 (2010), https://doi.org/10.1088/1748-3182/5/2/026007.
[13] C. Tang, B. Du, S. Jiang, Q. Shao, X. Dong, X.-J. Liu, H. Zhao, A pipeline inspection robot for navigating tubular environments in the sub-centimeter scale,, Sci Robot. (2022), https://doi.org/10.1126/scirobotics.abm85.
[14] G.K. Lau, H.T. Lim, J.Y. Teo, Y.W. Chin, Lightweight mechanical amplifiers for rolled dielectric elastomer actuators and their integration with bio-inspired wing flappers, Smart Mater. Struct. 23 (2014), https://doi.org/10.1088/0964-1726/23/2/025021.
[15] M. Ghilardi, H. Boys, P. Török, J.J.C. Busfield, F. Carpi, Smart lenses with electrically tuneable astigmatism, Sci. Rep. 9 (2019), https://doi.org/10.1038/s41598-019-52168-8.
[16] C.T. Nguyen, H. Phung, T.D. Nguyen, H. Jung, H.R. Choi, Multiple-degrees-of-freedom dielectric elastomer actuators for soft printable hexapod robot, Sens Actuators A Phys. 267 (2017) 505–516, https://doi.org/10.1016/j.sna.2017.10.010.
[17] A.T. Asbeck, S.M.M. De Rossi, I. Galiana, Y. Ding, C.J. Walsh, Stronger, smarter, softer: next-generation wearable robots, IEEE Robot Autom. Mag. 21 (2014) 22–33, https://doi.org/10.1109/MRA.2014.2360283.
[18] R.F. Shepherd, F. Ilievski, W. Choi, S.A. Morin, A.A. Stokes, A.D. Mazzeo, X. Chen, M. Wang, G.M. Whitesides, Multigait soft robot, Proc. Natl. Acad. Sci. 108 (2011) 20400–20403, https://doi.org/10.1073/pnas.1116564108.
[19] S.A. Morin, R.F. Shepherd, S.W. Kwok, A.A. Stokes, A. Nemiroski, G.M. Whitesides, Camouflage and display for soft machines, Science (1979) 337 (2012) 828–832, https://doi.org/DOI: 10.1126/science.1222149.
[20] A.D. Marchese, R.K. Katzschmann, D. Rus, A recipe for soft fluidic elastomer robots, Soft Robot 2 (2015) 7–25, https://doi.org/10.1089/soro.2014.0022.
[21] N.W. Bartlett, M.T. Tolley, J.T.B. Overvelde, J.C. Weaver, B. Mosadegh, K. Bertoldi, G.M. Whitesides, R.J. Wood, A 3D-printed, functionally graded soft robot powered by combustion, Science (1979) 349 (2015) 161–165, https://doi.org/DOI: 10.1126/science.aab0129.
[22] T. Li, G. Li, Y. Liang, T. Cheng, J. Dai, X. Yang, B. Liu, Z. Zeng, Z. Huang, Y. Luo, Fast-moving soft electronic fish, Sci. Adv. 3 (2017), e1602045 https://doi.org/DOI: 10.1126/sciadv.1602045.
[23] G. Li, X. Chen, F. Zhou, Y. Liang, Y. Xiao, X. Cao, Z. Zhang, M. Zhang, B. Wu, S. Yin, Y. Xu, H. Fan, Z. Chen, W. Song, W. Yang, B. Pan, J. Hou, W. Zou, S. He, X. Yang, G. Mao, Z. Jia, H. Zhou, T. Li, S. Qu, Z. Xu, Z. Huang, Y. Luo, T. Xie, J. Gu, S. Zhu, W. Yang, Self-powered soft robot in the Mariana Trench, Nature 591 (2021) 66–71, https://doi.org/10.1038/s41586-020-03153-z.
[24] J. Cao, L. Qin, J. Liu, Q. Ren, C.C. Foo, H. Wang, H.P. Lee, J. Zhu, Untethered soft robot capable of stable locomotion using soft electrostatic actuators, Extrem. Mech. Lett. 21 (2018) 9–16, https://doi.org/10.1016/j.eml.2018.02.004.
[25] K. Jung, K.J. Kim, H.R. Choi, A self-sensing dielectric elastomer actuator, Sens Actuators A Phys. 143 (2008) 343–351, https://doi.org/10.1016/j.sna.2007.10.076.
[26] T.A. Gisby, B.M. O'Brien, I.A. Anderson, Self sensing feedback for dielectric elastomer actuators, Appl. Phys. Lett. 102 (2013).

[27] Z. Ye, Z. Chen, Self-sensing of dielectric elastomer actuator enhanced by artificial neural network, Smart Mater. Struct. 26 (2017), 095056 https://doi.org/DOI 10.1088/1361-665X/aa7e66.
[28] T. Hoffstadt, M. Griese, J. Maas, Online identification algorithms for integrated dielectric electroactive polymer sensors and self-sensing concepts, Smart Mater. Struct. 23 (2014), https://doi.org/10.1088/0964-1726/23/10/104007.
[29] G. Rizzello, D. Naso, A. York, S. Seelecke, A self-sensing approach for dielectric elastomer actuators based on online estimation algorithms, IEEE/ASME Trans. Mechatron. 22 (2016) 728–738, https://doi.org/10.1109/TMECH.2016.2638638.
[30] R. Zhang, P. Iravani, P. Keogh, Closed loop control of force operation in a novel self-sensing dielectric elastomer actuator, Sens Actuators A Phys. 264 (2017) 123–132, https://doi.org/10.1016/j.sna.2017.08.013.
[31] G. Rizzello, F. Fugaro, D. Naso, S. Seelecke, Simultaneous self-sensing of displacement and force for soft dielectric elastomer actuators, IEEE Robot Autom. Lett. 3 (2018) 1230–1236, https://doi.org/10.1109/LRA.2018.2795016.
[32] B. O'Brien, J. Thode, I. Anderson, E. Calius, E. Haemmerle, S. Xie, Integrated extension sensor based on resistance and voltage measurement for a dielectric elastomer, in: Electroactive Polymer Actuators and Devices (EAPAD) 2007, SPIE (2007), 652415, https://doi.org/10.1117/12.715823.
[33] M. Rosenthal, N. Bonwit, C. Duncheon, J. Heim, Applications of dielectric elastomer EPAM sensors, in: Electroactive Polymer Actuators and Devices (EAPAD) 2007, SPIE (2007), 65241F, https://doi.org/10.1117/12.715084.
[34] B. Fasolt, M. Hodgins, G. Rizzello, S. Seelecke, Effect of screen printing parameters on sensor and actuator performance of dielectric elastomer (DE) membranes, Sens Actuators A Phys. 265 (2017) 10–19, https://doi.org/10.1016/j.sna.2017.08.028.
[35] A.T. Mathew, S.J.A. Koh, Operational limits of a non-homogeneous dielectric elastomer transducer, Int J. Smart Nano Mater. 8 (2017) 214–231, https://doi.org/10.1080/19475411.2017.1421276.
[36] M. Adachi, K. Hamazawa, Y. Mimuro, H. Kawamoto, Vibration transport system for lunar and Martian regolith using dielectric elastomer actuator, J. Electro 89 (2017) 88–98, https://doi.org/10.1016/j.elstat.2017.08.003.
[37] S. Hau, G. Rizzello, S. Seelecke, A novel dielectric elastomer membrane actuator concept for high-force applications, Extrem. Mech. Lett. 23 (2018) 24–28, https://doi.org/10.1016/j.eml.2018.07.002.
[38] H. Zhang, M.Y. Wang, J. Li, J. Zhu, A soft compressive sensor using dielectric elastomers, Smart Mater. Struct. 25 (2016), 035045, https://doi.org/10.1088/0964-1726/25/3/035045.
[39] T. Beckers, An Introduction to Gaussian Process Models, arXiv preprint arXiv: 2102.05497 (2021), https://doi.org/10.48550/arXiv.2102.05497.
[40] H. Kim, H. Chang, H. Shim, Model Reference Gaussian Process Regression: Data-Driven State Feedback Controller, ArXiv Preprint ArXiv:2303.09828 (2023), https://doi.org/10.48550/arXiv.2303.09828.
[41] A. Botchkarev, Evaluating performance of regression machine learning models using multiple error metrics in azure machine learning studio, SSRN (2018), 3177507, https://doi.org/10.2139/ssrn.3177507.

Dip Kumar Saha is currently pursuing his PhD in Engineering at the University of Sussex. He received his B.Sc. and M.Sc. in Mechanical Engineering from Rajshahi University of Engineering Technology (RUET), Bangladesh. His research interests include the sensorization of soft robotics, tactile sensing, and machine learning.

Hareesh Godaba received his B.Tech.(Hons.) degree from the Indian Institute of Technology (IIT) Bhubaneswar, Bhubaneswar, India, in 2013, and his Ph.D. degree from the National University of Singapore (NUS), Singapore, Singapore, in 2018, both in mechanical engineering. He is currently a Lecturer in Engineering with the Department of Engineering and Design, University of Sussex, Sussex, U.K. From 2018–2020, he was a postdoctoral research associate at the Queen Mary University of London. His primary research interests include soft robotics, electroactive technologies, and tactile sensing.